Towards CNC Automation in AFM Probe-Based Nano Machining

ICOMM 2013 95

E.B. Brousseau[1], B. Arnal[2], S. Thiery[3], E. Nyiri[4], O. Gibaru[5] and J.R. Mayor[6]

[1]Cardiff School of Engineering, Cardiff University, UK; brousseaue@cf.ac.uk•

[2]Arts et Metiers ParisTech, France; benoit.arnal@gadz.org

[3] LSIS, Arts et Metiers ParisTech & NON-A INRIA-Lille Nord Europe, France; stephane.thiery@ensam.eu

[4] LSIS, Arts et Metiers ParisTech, France; eric.nyiri@ensam.eu

[5] LSIS, Arts et Metiers ParisTech & NON-A INRIA-Lille Nord Europe, France; olivier.gibaru@ensam.eu

[6] Woodruff School of Mechanical Engineering, Georgia Institute of Technology, USA; rhett.mayor@me.gatech.edu

Key Words: AFM probe-based machining, CAD/CAM, automation, nanomanufacturing

ABSTRACT

This paper presents a feasibility study, which aims to demonstrate the applicability of the CNC automation philosophy for the process of AFM probe-based nano machining conducted on commercial AFM instruments. In particular, it is proposed to machine in this way nanostructures generated with any CAD software via the representation of tip path trajectories with G-code instructions. Such a representation can then be interpreted with a post processor at the interface of an AFM instrument. To demonstrate the validity of the proposed approach, it was implemented on a complex pattern. The results obtained open further research perspectives with respect to minimizing the sources of machining errors observed.

INTRODUCTION

Although the Atomic Force Microscope (AFM) was originally developed for the purpose of imaging and characterizing specimens at the nano scale [1], numerous researchers have used such an instrument in the last 20 years as a platform for various nano fabrication tasks [2]. As a result, AFM probe-based techniques have been proposed to enable processes such as nano manipulation [3], deposition [4] and removal of material [5]. This latter technique for structuring surfaces at the nano scale relies on the mechanical modification of material caused by the direct contact between the tip of an AFM probe and the sample surface as shown in Fig. 1.

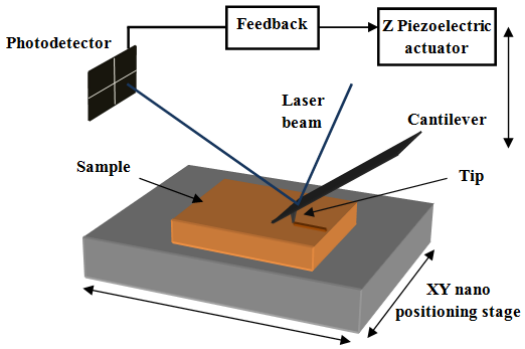

Fig. 1: AFM probe-based machining principle

More specifically, when performing this process, the tip of an AFM probe is brought into contact with a sample/workpiece until a predefined load is reached. Then the workpiece is moved relative to the tip via linear piezoelectric actuators, which generate displacements of the stage along the X and Y axes with sub-micrometer resolution. According to Hooke's law, the normal force applied by the tip on a workpiece depends on the deflection of the probe's cantilever in the normal direction at the tip position. This deflection is normally measured by projecting a laser beam on the cantilever and by monitoring the displacement of the beam reflection with a photodetector. The photodetector output signal can be used to implement a feedback loop to maintain a constant cantilever deflection as the tip moves across the sample surface. This is achieved by adjusting constantly the vertical displacement of the probe with a linear piezoelectric actuator on which the probe is attached.

The attractive characteristic of AFM probe-based mechanical machining is that the process is relatively simple and low-cost to implement [6]. In addition, it has shown high flexibility in producing complex three dimensional (3D) features and has been applied for cutting a wide range of engineering materials such as metals, semiconductors and polymers [7].

Given that AFM instruments were, and still are, primarily designed for imaging tasks, by default, the typical path followed by the tip of an AFM probe implements a raster scan strategy. Although some AFM manufacturers provide software modules to perform lithography operations, such solutions can be limited with respect to 1) the range of tip motions that can be developed, 2) the flexibility in realizing purposely-defined tip displacement strategies and 3) their portability for easily transferring trajectories data between different AFM instruments. As a result, in order to conduct particular AFM-based nano fabrication operations many researchers have had to implement customized procedures and computer routines enabling the realization of a large variety of tip trajectories. In this context, it would be advantageous for future tip-based nano fabrication studies to develop more automated, portable and flexible solutions that could enable 1) the path of AFM tips to be defined via widespread design software tools and 2) the implementation of such tip trajectories to be con-

• corresponding author

ducted on a broad range of AFM instruments. Unfortunately, efforts in this direction have only been conducted by a few researchers in recent years.

In particular, Horkas and co-workers implemented an AFM software with built-in functionalities for lithography applications [8]. In this work, a specifically-designed CAD interface was developed to enable the drawing of tip trajectories by the user, which could subsequently be sent to the controller of an AFM instrument. In [9], the authors developed an AFM nanolithography software with a purposely-built graphical user interface for designing patterns. An attempt was made at improving the portability of stored tip trajectory data by representing them as functions in a Windows meta file. Other authors proposed a solution that linked a commonly used CAD software with an AFM [10]. To achieve this, a CAM software was modified to read CAD drawings of nano patterns and translate them into proprietary tip trajectory data. A common drawback of these proposed approaches is that they do not offer a solution where the generation of the machining paths can be achieved in a fully automated manner while enabling the design and path planning steps to be carried out without purposely-built software tools. In contrast, Johannes et al. implemented a nano scale design environment for AFM anodization by incorporating conventional CAD/CAM software [11, 12]. The interesting aspect of this work is that the G-code file format was used to communicate the tip paths to an AFM controller.

In the case of material removal operations performed with the tip of an AFM probe, the most promising approach to enable increased flexibility and automation of the design and machining tasks is that reported above by Johannes and co-workers. In particular, given the maturity of existing CAD/CAM solutions which enable the seamless integration of 3D modeling and tool path planning steps in conventional cutting processes, it is natural to reuse such an approach for the purpose of automating AFM probe-based nano machining tasks. Besides, this approach could contribute to the development of a more flexible and portable solution for nanofabrication tasks which would not be restricted to particular customized software or AFM instruments. In this context, the purpose of the research presented in this paper was to follow the method put forward by Johannes and co-workers in the context of nano machining operations rather than anodization lithography. In particular, the objective of this research is to demonstrate the feasibility of establishing a link between CAD and AFM probe-based nano machining via the development of a G-code post processor for the AFM equipment controller that will interpret the G-code representation of tip path trajectories generated using CAM software.

CAD/CAM APPROACH FOR AFM PROBE-BASED NANO MACHINING

A. METHODOLOGY

Fig. 2 illustrates the CAD/CAM approach followed in this

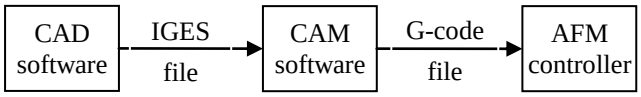

Fig. 2: CAD/CAM approach adopted

study. It is proposed that the 3D models of the nano structures to be machined can be designed using any conventional CAD software. Next, a neutral file format, such as the Initial Graphics Exchange Specification (IGES) data format, can be utilized to transfer design data to a CAM software. Tip path trajectories can then be automatically defined with the path generation functionalities provided by such software. In particular, parameters such as the distance between two grooves (i.e. the step-over), the cut direction, the tolerance and the tool geometry are provided by the user when defining the tip paths. The data created in this way can then be represented by a set of G-code instructions and be communicated to the controller of an AFM instrument. G-code is a widely used computer numerical control (CNC) programming language and thus, it is implemented by commonly found CAM software. When deploying this approach with a particular AFM instrument, it is necessary for the user to develop a post-processor that can translate the G-code format into instructions that can be understood by the AFM controller. This is required as conventional AFM systems have not been developed with the primary purpose of conducting nano machining operations and understandably, they do not have built-in capabilities to read G-code input.

B. IMPLEMENTATION

In this work, the particular CAD and CAM software used were SolidWorks and PowerMill respectively. The AFM instrument utilized was the XE-100 model from Park Systems. A post-processor was developed to translate G-code data into instructions for the AFM controller using C++ libraries provided by Park Systems. The flow of data processing from the CAD software to the AFM controller is illustrated in Fig. 3.

The probes employed to perform the machining experiments were DNISP probes from Bruker (see Fig. 4). This type of AFM probe is normally employed for nano-indentation experiments. It is made of a cantilever in stainless steel on which a three sided diamond tip is glued. The particular AFM probe employed had a nominal normal spring constant of 221 $N.m^{-1}$ and the nominal tip radius specified was 40 nm.

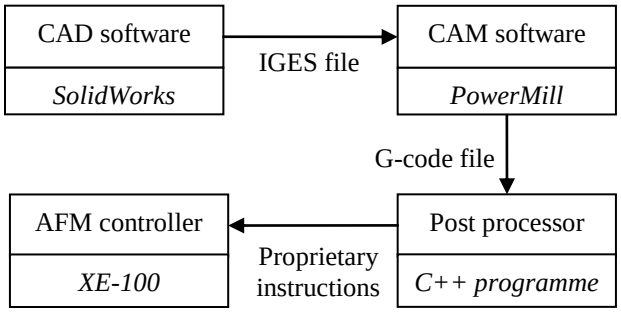

Fig. 3: Implementation of the CAD/CAM approach adopted

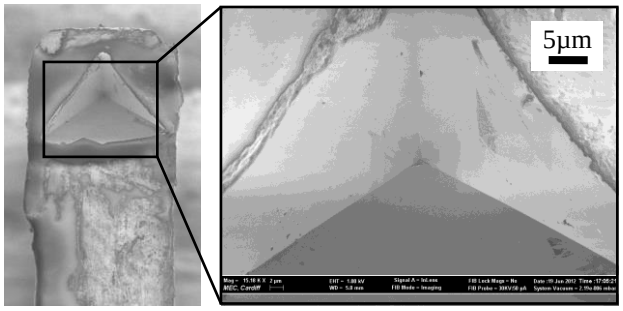

Fig. 4: AFM probe utilized

The workpiece processed was a dual phase brass alloy CuZn39Pb3 with dimensions 12 mm x 12 mm x 3 mm. Using wire electro discharge machining, this specimen was cut from an initial 4 inch brass circular wafer prepared with a succession of lapping and polishing steps. The surface roughness achieved in this way was Ra 20 nm as measured with a white light interferometer (MicroXAM-100-HR). The hardness of each phase present in the brass alloy was also measured using a micro hardness tester (Mitutoyo Micro-Vickers Hardness Tester HM-122). In this case, an average was calculated from five measurements conducted in each phase separately under a load of 10 g. For the α and β phases, the hardness was ~125 HV and ~ 203 HV respectively. It was decided to carry out the cutting operations only on grains corresponding to the α phase in order to avoid changes in the processing conditions that can be introduced from processing both phases simultaneously. In particular, it is known that for micro- and nano-scale cutting, the crystalline structure of processed materials has a significant influence on different machining characteristics [13, 14].

The initial development stage of the proposed approach revealed that its implementation with the particular AFM instrumentation used had two important constraints. The first one is the fact that the AFM controller could only generate the stage lateral displacements along four axes, namely in the directions perpendicular, parallel and at ± 45 degrees angle with respect to the orientation of the long axis of the cantilever. Thus, to execute G-code instructions between points as accurately as possible, the lines or curves representing the planned tip trajectories have to be discretized into smaller segments oriented along one of the four constrained directions mentioned above. This discretization step was achieved with the Bresenham's line algorithm, which is commonly used in computer graphic applications. Fig. 5 illustrates the implementation of this algorithm for approximating a line which does not follow one of the axes of constrained displacements. Fig. 6 shows the results of implementing this approach when machining grooves with a normal applied force of 35 µN and with discretization steps comprised between 50 nm and 1 µm. Each groove shown is 23 µm in length and orientated at 30 degrees with respect to the long axis of the cantilever. This figure illustrates the deviation of the machined grooves from a linear line as a function of the discretization step used with the Bresenham algorithm. In particular, as the value of this step increases, the deviation

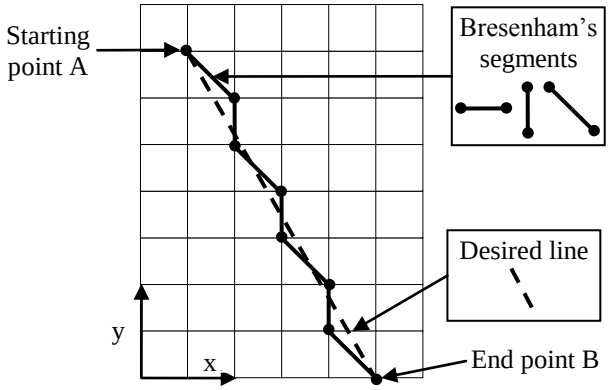

Fig. 5: Illustration of the Bresenham's line algorithm

from a linear line becomes more pronounced and the individual Bresenham segments more observable.

The second constraint imposed by the instrumentation used was that a time delay, in the order of a second, takes place between the machining of each Bresenham segments. More specifically, this time delay occurs every time the particular C++ function employed to generate the lateral displacement of the stage is called. This means that machining is interrupted between each segment. Thus, this influences the time required to cut a given pattern depending on the resolution of the discretization step selected. Consequently, a compromise should be found between the desired accuracy of the machined pattern and the machining efficiency. The time taken to machine a segment of 1 µm in length including the imposed delay was measured and based on this, it was possible to empirically derive the speed of progression of the AFM tip, v, in µm.min^{-1} as a function of the discretization step, p, expressed in µm:

$$v = 45 \, . \, p \qquad (1)$$

Thus, from the experimental results shown in Fig. 6, if a minimum discretization step of 100 nm is chosen for any pattern to be cut, then the maximum cutting speed achievable in this case is 4.5 µm.min^{-1}, which is particularly slow. However, the deployment of the proposed CAD/CAM approach on different AFM systems may not necessarily be limited by the constraints reported here, and in such cases, higher cutting speeds could be achieved.

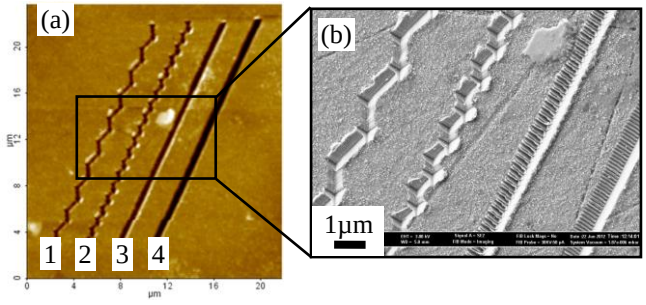

Fig. 6: Grooves machined using the Bresenham algorithm with different discretization steps: (a): AFM image, (b): SEM image. The discretization steps indicated on (a) are: groove (1): 1 µm, (2): 500 nm; (3): 100 nm and (4): 50 nm

In order to examine more closely the quality of the achieved grooves with different discretization steps, another experi-

ment was carried out where 25 µm lines were cut in the direction parallel to and towards the cantilever (see Fig. 7). From this figure, pile-ups within the grooves can be clearly noticed when using a discretization step above 200 nm. This is due to the interruption of the tip progression between each Bresenham segment. To explain this, the load acting on tip is considered during both of the successive processing stages. In particular, the first stage corresponds to a static case when the tip is engaged vertically into the material without the lateral displacement while the second, dynamic, stage describes the lateral progression of the tip into the material according to the cutting direction shown in Fig. 7.

The first case can be thought of as a nanoindentation operation when the tip has reached its maximum penetration depth during the loading cycle. In this situation, the only force acting on the tip is considered to be normal to the material surface and it is referred to as F_n. Thus, based on the Euler-Bernoulli cantilever beam theory, the vertical displacement, z_c, of the free end of the probe cantilever can be expressed as follows:

$$z_c = \frac{F_n . L^3}{3EI} \tag{2}$$

where L is the length of the cantilever, E is its modulus of elasticity and I is its second moment of area.

In the second case, an additional force, F_c, acting on the end of the tip and oriented horizontally is considered. This force is the consequence of the interaction between the tip and the material as the probe is moved laterally with respect to the workpiece. Depending on the machining conditions, this interaction is the result of the particular processing regime that can take place namely, adhering, ploughing or cutting. In this case, the moment, M_c, that occurs at the free end of the cantilever and which is caused by F_c acting on the tip must be taken into account in the expression of z_c:

$$z_c = \frac{F_n . L^3}{3EI} + \frac{M_c . L^2}{2EI} \tag{3}$$

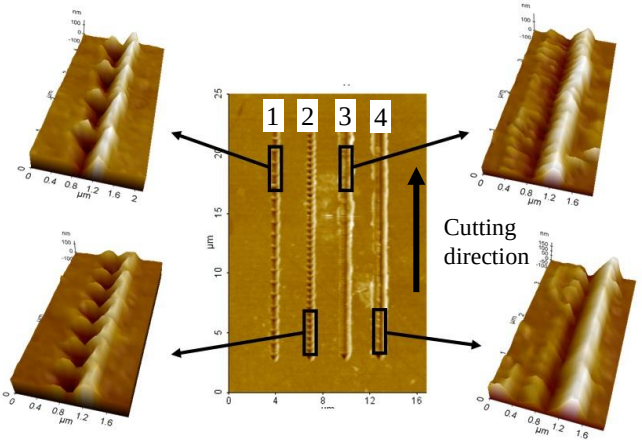

Fig. 7: Effect of the discretization step on the quality of the grooves. The discretization steps indicated are: groove (1): 1 µm, groove (2): 500 nm; groove (3): 200 nm and groove (4): 100 nm

Fig. 8 illustrates the loads considered on the free end of the probe cantilever using the notations introduced. Equation (3) can also be written as follows by defining l_t as the length of the probe tip:

$$z_c = \frac{F_n . L^3}{3EI} + \frac{F_c . l_t . L^2}{2EI} \tag{4}$$

Thus, the vertical displacement, z_c, of the free end of the cantilever is described by equation (2) when the machining process is interrupted between the Bresenham segments and by equation (4) when the tip progresses along such segments. It is important to note that, for the first static case, a simplification is made by assuming that the force acting on the probe tip has only a vertical component, F_n. In reality, a horizontal force component should also be taken into account. This is due to the fact that, following the lateral progression of the probe into the workpiece, the area of contact between the tip and the material is not symmetrical with respect to the axis of the tip. However, in the explanations reported here, it is assumed that this load can be neglected in comparison with the force F_c, which is generated during the probe lateral displacement.

It is also important to keep in mind that the feedback loop of the AFM system ensures that the vertical position, z_l, of the laser beam reflected from the back of the free end of the cantilever on the photodiode is kept constant during the engagement of the tip with the material. It is considered that z_l is directly proportional to the vertical movement of the free end of the cantilever, z_c. Thus, for the first case, when the machining operation is interrupted, z_l is formulated as follows:

$$z_l = c.(\frac{F_n . L^3}{3EI}) \tag{5}$$

While, during the lateral displacement of the probe, z_l is expressed according to equation (6) below:

$$z_l = c.(\frac{F_n . L^3}{3EI} + \frac{F_c . l_t . L^2}{2EI}) \tag{6}$$

Therefore, in order to keep z_l constant throughout machining and thus, to ensure that the values obtained from equations (5) and (6) are equal over time, the feedback loop of the AFM system controls the vertical position of the cantilever via the piezoelectric actuator on which the probe is mounted. In particular, as the processing condition changes from a static status (i.e. during the time spent between Bresenham segments) to a dynamic one, the piezoelectric actuator raises the probe in order to decrease the value of F_n as a result of the added contribution from F_c. Conversely, as the status of processing is changed from a dynamic to a static condition, the probe is lowered in order to increase the contribution from F_n.

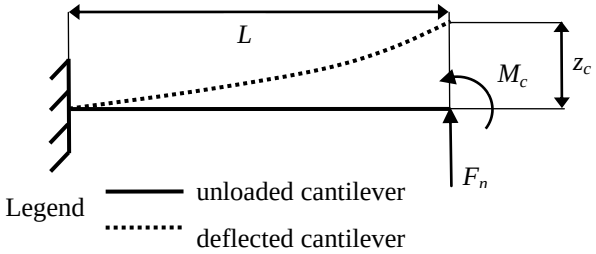

Fig. 8: Schematic of the probe cantilever with the considered loads acting at its free end during the lateral progression of the tip into the material

The consequence of successively raising and lowering the probe can also be seen in Fig. 9, which shows obtained profiles in the cutting direction along the bottom of the grooves processed with Bresenham discretization steps of 1 µm (Fig. 9(a)) and 200 nm (Fig. 9(b)). In particular, regularly spaced indents with higher depths are observed along each groove at positions referred to as x_i, x_{i+1}, …, in this figure. These indents correspond to points where the processing interruptions took place and which are associated with a predominant load contribution from F_n. The formation of pile-ups on either side of these indents is clearly visible in Fig. 9(a). In this case, a higher pile-up is formed in front of the tip, which corresponds to a region where no prior plastic deformation took place. In addition, the average depth of the generated indents reduces as the discretization step is decreased. This observation could be due to the fact that, below a given discretization length, the indents are formed over the pile-up created during the preceding nanoindentation. In particular, from the data shown in Fig. 7, it was estimated that the distance between the bottom of an indent and the height of the neighboring pile-ups is between 200 nm and 400 nm. Thus, with a discretization step within or below this range, the depth of the indent achieved could be affected by strain hardening of the pile-up material generated from the preceding nanoindentation operation. However, further studies, which are outside the scope of this paper, should be conducted to investigate this hypothesis.

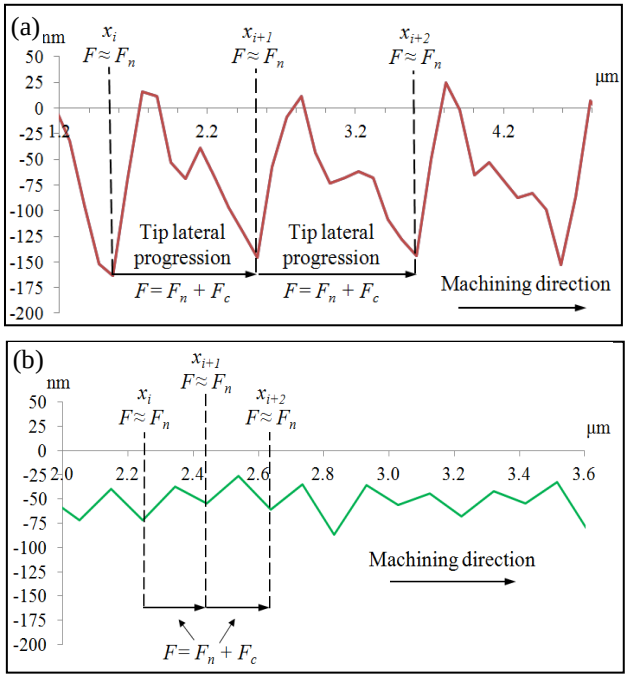

Fig. 9: Grooves profile with discretization steps of (a) 1 µm and (b) 200 nm

In the next section, the validity of the CAD/CAM approach proposed will be demonstrated by applying it with a particular example.

DEMONSTRATION OF THE CAD/CAM APPROACH

A. MACHINING PATTERN

In order to illustrate the validity of the implemented CAD/CAM approach for AFM probe-based nano machining, a relatively complex pattern representing half of a snow flake was designed and subsequently machined on the brass workpiece. The G-code instructions that were used to process this pattern are given in the appendix. Based on the initial set of experiments reported in the previous section, it was decided to process this pattern with an applied force of 35 µN and a discretization step of 100 nm. Fig. 10 shows its theoretical geometry using this discretization and Fig. 11 shows a SEM image of the obtained result. This figure also indicates the orientation of the cantilever with respect to the processed pattern as well as the machining direction followed between the start and end points, for which the coordinates are (0,10) on Fig. 10. In the next section, the errors between the obtained pattern and its theoretical geometry are estimated.

B. EVALUATION OF MACHINING ERRORS

An AFM scan (see Fig. 12) of the processed pattern was obtained with a resolution of 512 x 512 pixels by utilizing a second AFM probe (CSG30 from NT-MDT), which is designed for imaging purpose in contact mode. From this AFM scan, topographical data for all pixels could be subsequently extracted via an image processing software (XEI from Park Systems). More specifically, the (x, y, z) coordinates of each pixel were exported into a (3 x N) matrix, M_{Data}, with $N = 512^2 = 262144$.

Next, to extract information with respect to the location of the points located at the bottom of the achieved grooves, the columns in this matrix were ordered according to the value of their z coordinates as follows:

$$M_{Data} = \begin{pmatrix} x_1 & x_2 & \dots & x_N \\ y_1 & y_2 & \dots & y_N \\ z_1 & z_2 & \dots & z_N \end{pmatrix} \quad \text{with } z_i < z_j \tag{7}$$

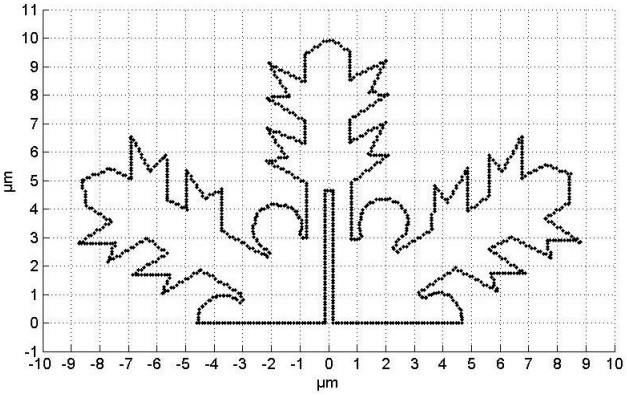

Fig. 10: Theoretical geometry of the designed pattern

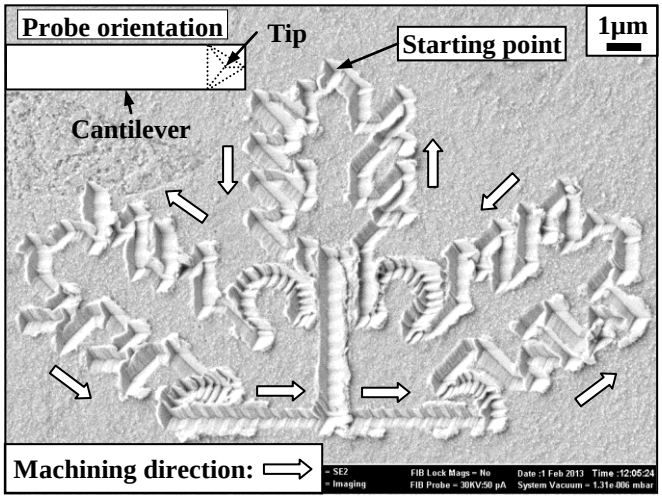

Fig. 11: SEM image of the pattern cut with AFM probe-based machining.

In addition, the (X, Y) coordinates of the theoretical geometry shown in Fig. 10 were stored in a (2 x M) matrix, M_{Model}, with M = 1157, which corresponds to the number of discretization points:

$$M_{Model} = \begin{pmatrix} X_1 & X_2 & \dots & X_M \\ Y_1 & Y_2 & \dots & Y_M \end{pmatrix} \tag{8}$$

Due to the fact that the coordinate systems used to define the points stored in both matrices are different, it is required to fit the (x, y) values of the points in M_{Data} to those in M_{Model} prior to estimating the machining errors. This was achieved using an Iterative Closest Point (ICP) algorithm developed and implemented in Matlab. In [15], the authors showed that this algorithm is robust in the context of shape verification. The convergence criterion utilized with this algorithm is the minimization of the sum of the square errors between the data points and the closest model points. Thus, the data fitted can be expressed as:

$$\forall i = 1 \dots N$$
$$\begin{pmatrix} x_i^* \\ y_i^* \end{pmatrix} = \begin{pmatrix} cos(\theta) & -sin(\theta) \\ sin(\theta) & cos(\theta) \end{pmatrix} \begin{pmatrix} x_i \\ y_i \end{pmatrix} + \begin{pmatrix} T_x \\ T_y \end{pmatrix} = R \begin{pmatrix} x_i \\ y_i \end{pmatrix} + T \tag{9}$$

where the rotation matrix, R, and the translation vector, T, applied to the data are the outputs of the ICP algorithm. In this way, a matrix, M_{Data_Fitted} could be generated to store the new coordinates of each pixel for the scanned AFM data:

$$M_{Data\_Fitted} = \begin{pmatrix} x_1^* & x_2^* & \dots & x_N^* \\ y_1^* & y_2^* & \dots & y_N^* \\ z_1 & z_2 & \dots & z_N \end{pmatrix} \text{with } z_i < z_j \tag{10}$$

Fig. 13 shows the results of the fitting procedure for a set of S deepest data points, i.e. by selecting the first S columns of M_{Data}. In this case, S was equal to 11682, which correspond to a depth threshold of 105.3 nm below the surface of the brass workpiece. This number of points was chosen in order to avoid including data that did not belong to the machined pattern and thus may affect the fitting accuracy. In this case,

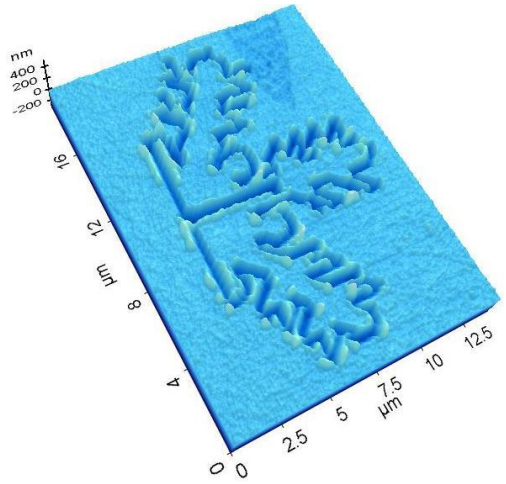

Fig. 12: AFM image of the obtained pattern

the translation vector obtained was (T_x, T_y) = (10.967, -5.648) in micrometres and the angle of rotation was θ = 2.193 degrees.

Following this procedure, the trajectory followed by the tip during machining could be obtained by extracting a subset of the coordinates in M_{Data_Fitted}, which are those corresponding to points at the bottom of the grooves. To achieve this, another algorithm was implemented to select the deepest point in the matrix of fitted data, M_{Data_Fitted}, within a large set of neighboring pixels for each model point. The most accurate results were achieved by choosing sets of points made of 15 x 15 pixels centered on the closest pixel for each model point. This choice was made based on statistical observations conducted on larger sets of pixels in order to identify the global maximum value for the machining error. More specifically, the value for this error was found to be 245 nm. Given that the pixel size is 39 nm x 39 nm, using a length of 7 pixels in each direction for the search around a central point was sufficient to find the maximum error and thus, the set of tip trajectory points. In this way, the points identified to belong to the deepest part of the grooves were those selected several times with the algorithm. Fig. 14 shows the results of implementing this algorithm for extracting the trajectory followed by the tip during machining. This figure also provides a comparison between the theoretical geometry and the trajectory achieved by the tip. The algorithm extracted 367 different points from M_{Data_Fitted} that belonged to the tip trajectory at the bottom of the machined pattern.

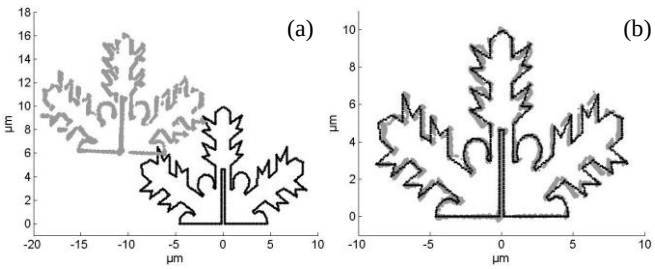

Fig. 13: The model (darker color) and the S deepest points (grey color) for the pattern (a) before and (b) after the fit

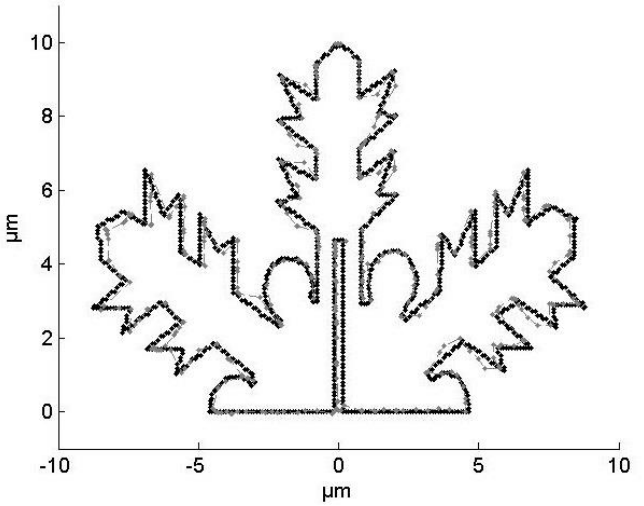

Fig. 14: Comparison of the tip trajectory achieved (grey color) with the theoretical one (black color).

A statistical study conducted with these extracted points showed an average distance error to the model points equals to 91 nm while, as mentioned above, the maximum error was equal to 245 nm. Two sources of errors are suggested to explain the discrepancies observed. The first one is the possible error in the lateral displacements of the stage and the second one is linked to the fact that the probe used is not a rigid tool. In particular, the cantilever on which the tip is mounted is subjected to different amount of torsion and flexion as a function of the machining direction followed. Considering that the average width of the grooves of the machined pattern was estimated to be about 500 nm, an average error of 91 nm represents a relatively important error. Thus, future work should aim to characterize the sources of discrepancies. In particular, further studies should target the development of a predictive geometric error model that accounts for the anisotropic stiffness of the AFM machining probe in order to implement corrections for the trajectory that takes into account the mechanical behavior of the cantilever.

CONCLUSIONS

The aim of this study was to demonstrate the feasibility of integrating widespread CAD/CAM solutions with an AFM instrument in order to conduct AFM probe-based nano machining operations. Through the utilization of such software tools and commonly used file formats for software communication, it is possible to provide a high level of automation and flexibility for AFM machining tasks. It is anticipated that such an approach will enable the further study of the influence of strategies for tip trajectories on the efficiency and quality of the obtained patterns when machining at such small scale. The reported research highlighted issues with respect to the occurrence of location errors for the machined structures. It is suggested that these issues are strongly dependent on the fact that the process relies on flexible tools for the cutting operations. Thus, further studies aimed at reducing such machining errors should account for the behavior of the cantilever on which the tip is mounted. Finally, it was also observed that the machining interruptions that are characteristics of the particular implementation reported lead to the main plastic deformation mechanism being dominated by a series of nano indentation operations. This peculiarity could be exploited further to automate the generation of surfaces with ordered nanostructures in the shape of inverted pyramids.

REFERENCES

[1] G. Binnig, C.F. Quate, and Ch. Gerber, "Atomic Force Microscope," *Physical Review Letters*, 1986; 56(9): 930-934.

[2] A.A. Tseng, A. Notargiacomo, and T.P. Chen, "Nanofabrication by scanning probe microscope lithography: a review," *J. Vac. Sci. Technol. B*, 2005; 23(3): 877-894.

[3] F. Krohs, C. Onal, M. Sitti, and S. Fatikow, "Towards automated nanoassembly with the atomic force microscope: A versatile drift compensation procedure," *ASME Trans. J. of Dynamic Sys., Meas. and Control*, 2009; 131(6): 1-8.

[4] R.D. Piner, J. Zhu, F. Xu, S. Hong, and C.A. Mirkin, "Dip Pen Nanolithography," *Science*, 1999; 283(5402): 661-663.

[5] A. Notargiacomo, V. Foglietti, E. Cianci, G. Capellini, M. Adami, P. Faraci, F. Evangelisti, and C. Nicolini, "Atomic force microscopy lithography as a nanodevice development technique," *Nanotechnology*, 1999; 10: 458-463.

[6] B.A. Gozen and O.B. Ozdoganlar, "Design and evaluation of a mechanical nanomanufacturing system for nanomilling," *Precision Engineering*, 2012; 36(1): 19-30.

[7] E.B. Brousseau, F. Krohs, E. Caillaud, S. Dimov, O. Gibaru, and S. Fatikow, "Development of a novel process chain based on atomic force microscopy scratching for small and medium series production of polymer nano structured components," *ASME Trans. Int. J. Mfg. Sci.*, 2010; 132(3): 030901 (8pp).

[8] I. Horcas, R. Fernández, J.M. Gómez-Rodríguez, J. Colchero, J. Gómez-Herrero, and A.M. Baro, "WSXM: a software for scanning probe microscopy and a tool for nanotechnology," *Review of Scientific Instruments*, 2007; 78: 013705.

[9] J. Lekki, S. Kumar, S.S. Parihar, S. Grange, C. Baur, R. Foschia, and A. Kulik, "Data coding tools for color-coded vector lithography," *Review of Scientific Instruments*, 2004; 75(11): 4646-4650.

[10] S. Cruchon-Dupeyrat, S. Porthun, and G.-Y. Liu, "Nanofabrication using computer-assisted design and automated vector-scanning probe lithography," *Applied Surface Science*, 2001; 175-176: 636-642.

[11] M.S. Johannes, J.F. Kuniholm, D.G. Cole, and R.L. Clark, "Automated CAD/CAM-based nanolithography using a custom atomic force microscope," *IEEE Trans. Automation Sci. and Eng.*, 2006; 3(3): 236-239.

[12] M.S. Johannes, D.G. Cole, and R.L. Clark, "Three-dimensional design and replication of silicon oxide nanostructures using an atomic force microscope," *Nanotechnology*, 2007; 18(34): 345304 (7pp).

[13] X. Liu, R.E. DeVor, S.G. Kapoor, and K.F. Ehmann, "The mechanics of machining at the micro-scale: assessment of the current state of the science," *ASME Trans. J. Manuf. Sci. Eng.*, 2004, 126(4): 666-678.

[14] H. Weule, V. Huntrup, and H. Tritschle, "Micro-cutting of steel to meet new requirements in miniaturisation," *CIRP Annals*, 2001, 50: 61-64.

[15] P. Bergström, S. Rosendahl, and M. Sjödahl, "Shape verification aimed for manufacturing process control", *Optics and Lasers in Engineering*, 2011, 49(3): 403-409.

The Matlab ICP algorithm can be downloaded for free at http://www.mathworks.com/matlabcentral/fileexchange/ 12627.

APPENDIX: G-CODE USED FOR MACHINING THE SNOW FLAKE PATTERN

```
G90
F0.5
G0 Z-1
G0 X9.98000 Y-0.01660 Z-1
G1 X9.98000 Y-0.01660 Z1
G1 X9.41080 Y0.82390 Z1
G1 X8.48640 Y0.82520 Z1
G1 X9.11280 Y2.09730 Z1
G1 X7.95210 Y1.38200 Z1
G1 X7.89330 Y2.15160 Z1
G1 X7.10750 Y0.82390 Z1
G1 X6.30030 Y0.82520 Z1
G1 X6.83640 Y2.15160 Z1
G1 X5.80420 Y1.46200 Z1
G1 X5.69830 Y2.17880 Z1
G1 X4.91250 Y0.76950 Z1
G1 X2.98830 Y0.76950 Z1
G1 X2.98830 Y0.90510 Z1
G1 X3.12390 Y0.98630 Z1
G1 X3.28650 Y0.93220 Z1
G1 X3.50320 Y0.94750 Z1
G1 X3.70630 Y1.01240 Z1
G1 X3.90980 Y1.14890 Z1
G1 X4.04540 Y1.31150 Z1
G1 X4.12660 Y1.55530 Z1
G1 X4.15500 Y1.81650 Z1
G1 X4.10060 Y2.14240 Z1
G1 X3.93690 Y2.39550 Z1
G1 X3.69330 Y2.57680 Z1
G1 X3.42200 Y2.63930 Z1
G1 X3.12680 Y2.62070 Z1
G1 X2.86720 Y2.52080 Z1
G1 X2.69030 Y2.36840 Z1
G1 X2.58190 Y2.17880 Z1
G1 X2.45760 Y2.07130 Z1
G1 X2.31770 Y2.15130 Z1
G1 X3.23230 Y3.75050 Z1
G1 X4.69560 Y3.75050 Z1
G1 X4.35570 Y4.30910 Z1
G1 X5.34600 Y4.97000 Z1
G1 X3.96390 Y4.94270 Z1
G1 X4.31620 Y5.64730 Z1
G1 X5.88800 Y5.70160 Z1
G1 X5.31460 Y6.22720 Z1
G1 X6.53850 Y6.89430 Z1
G1 X5.07500 Y6.89430 Z1
G1 X5.40020 Y7.65300 Z1
G1 X5.02090 Y8.60120 Z1
G1 X4.12660 Y8.46570 Z1
G1 X3.55750 Y7.59880 Z1
G1 X2.79860 Y8.73670 Z1
G1 X2.81720 Y7.46590 Z1
G1 X2.14830 Y7.70710 Z1
G1 X2.96140 Y6.35230 Z1
G1 X2.44630 Y5.64730 Z1
G1 X1.68760 Y6.83970 Z1
G1 X1.67830 Y5.55790 Z1
G1 X1.03720 Y5.81030 Z1
G1 X1.85020 Y4.45510 Z1
G1 X1.02890 Y3.08030 Z1
G1 X0.78920 Y3.00040 Z1
G1 X0.70930 Y3.10030 Z1
G1 X0.86910 Y3.26020 Z1
G1 X0.95590 Y3.45230 Z1
G1 X0.95590 Y3.69620 Z1
G1 X0.90180 Y3.94020 Z1
G1 X0.77920 Y4.19920 Z1
G1 X0.56950 Y4.41890 Z1
G1 X0.30970 Y4.55890 Z1
G1 X0.01000 Y4.61870 Z1
G1 X0.00023 Y0.13869 Z1
G0 X0.00023 Y0.13869 Z-1
G0 X0.0000 Y-0.16131 Z-1
G1 X0.0000 Y-0.16131 Z1
G1 X0.0000 Y-4.65200 Z1
G1 X0.23970 Y-4.62530 Z1
G1 X0.51950 Y-4.58540 Z1
G1 X0.69930 Y-4.46560 Z1
G1 X0.89910 Y-4.30570 Z1
G1 X0.97900 Y-4.14590 Z1
G1 X1.05900 Y-3.96270 Z1
G1 X1.04900 Y-3.77280 Z1
G1 X0.97900 Y-3.60300 Z1
G1 X0.88910 Y-3.39320 Z1
G1 X0.89910 Y-3.27330 Z1
G1 X1.05900 Y-3.15340 Z1
G1 X1.93140 Y-4.43360 Z1
G1 X1.11850 Y-5.89690 Z1
G1 X1.73820 Y-5.68430 Z1
G1 X1.74170 Y-6.87240 Z1
G1 X2.58190 Y-5.62570 Z1
G1 X3.01550 Y-6.41180 Z1
G1 X2.28370 Y-7.76670 Z1
G1 X2.90710 Y-7.64890 Z1
G1 X2.85290 Y-8.79660 Z1
G1 X3.66590 Y-7.57700 Z1
G1 X4.23490 Y-8.41710 Z1
G1 X5.23470 Y-8.46810 Z1
G1 X5.56290 Y-7.57700 Z1
G1 X5.10220 Y-6.76390 Z1
G1 X6.53850 Y-6.76390 Z1
G1 X5.31460 Y-6.05050 Z1
G1 X5.88800 Y-5.62570 Z1
G1 X4.45180 Y-5.59870 Z1
G1 X3.93690 Y-4.86710 Z1
G1 X5.42730 Y-4.86710 Z1
G1 X4.23570 Y-4.16250 Z1
G1 X4.80400 Y-3.70160 Z1
G1 X3.28650 Y-3.62060 Z1
G1 X2.49750 Y-2.38420 Z1
G1 X2.63730 Y-2.26440 Z1
G1 X2.83710 Y-2.36430 Z1
G1 X3.03690 Y-2.60400 Z1
G1 X3.22670 Y-2.73380 Z1
G1 X3.45660 Y-2.78380 Z1
G1 X3.68630 Y-2.76390 Z1
G1 X3.93600 Y-2.66400 Z1
G1 X4.12660 Y-2.53660 Z1
G1 X4.26210 Y-2.34690 Z1
G1 X4.34570 Y-2.06460 Z1
G1 X4.33560 Y-1.76490 Z1
G1 X4.23490 Y-1.45260 Z1
G1 X4.07230 Y-1.29010 Z1
G1 X3.82840 Y-1.12750 Z1
G1 X3.53030 Y-1.07560 Z1
G1 X3.23230 Y-1.10030 Z1
G1 X3.04700 Y-1.16550 Z1
G1 X2.93700 Y-1.00560 Z1
G1 X2.96140 Y-0.80220 Z1
G1 X4.93940 Y-0.80220 Z1
G1 X5.88800 Y-2.07590 Z1
G1 X5.93400 Y-1.39520 Z1
G1 X7.05330 Y-1.99460 Z1
G1 X6.34880 Y-0.74810 Z1
G1 X7.13460 Y-0.74810 Z1
G1 X8.00180 Y-2.04860 Z1
G1 X8.09190 Y-1.41520 Z1
G1 X9.22130 Y-1.99460 Z1
G1 X8.54370 Y-0.74810 Z1
G1 X9.51920 Y-0.74810 Z1
G1 X9.98000 Y-0.01660 Z1
G0 X9.98000 Y-0.01660 Z-1
G0 X0.000 Y-0.16131 Z-1
G1 X0.0000 Y-0.16131 Z1
G1 X4.64265 Y-0.16131 Z1
G1 X4.64265 Y0.13869 Z1
G1 X0.00023 Y0.13869 Z1
G0 X0.00023 Y0.13869 Z-1
```